ADVANCED MATERIALS
www.advmat.de

Modular Design of a Polymer-Bilayer-Based Mechanically Compliant Worm-Like Robot

Livius F. Muff, Austin S. Mills, Shane Riddle, Véronique Buclin, Anita Roulin, Hillel J. Chiel, Roger D. Quinn,* Christoph Weder,* and Kathryn A. Daltorio**

Soft earthworm-like robots that exhibit mechanical compliance can, in principle, navigate through uneven terrains and constricted spaces that are inaccessible to traditional legged and wheeled robots. However, unlike the biological originals that they mimic, most of the worm-like robots reported to date contain rigid components that limit their compliance, such as electromotors or pressure-driven actuation systems. Here, a mechanically compliant worm-like robot with a fully modular body that is based on soft polymers is reported. The robot is composed of strategically assembled, electrothermally activated polymer bilayer actuators, which are based on a semicrystalline polyurethane with an exceptionally large nonlinear thermal expansion coefficient. The segments are designed on the basis of a modified Timoshenko model, and finite element analysis simulation is used to describe their performance. Upon electrical activation of the segments with basic waveform patterns, the robot can move through repeatable peristaltic locomotion on exceptionally slippery or sticky surfaces and it can be oriented in any direction. The soft body enables the robot to wriggle through openings and tunnels that are much smaller than its cross-section.

1. Introduction

Biological inspiration has led to a plethora of soft robots that aim to replicate natural functionality and motility of invertebrates and soft-bodied animals such as snails,[1] jellyfish,[2,3] octopi,[4,5] caterpillars,[6,7] midge larvae,[8] and earthworms.[9,10] Earthwormlike robots are typically composed of a series of identical and radially symmetric segments that are actuated in specific wave patterns for high velocity or low cost of transport locomotion and which enable directional control.[11] Because of their ability to efficiently navigate through confined spaces and their modular and scalable architecture, such robots are ideal candidates for many applications that include search and rescue operations,[12] underground exploration,[13,14] pipe inspection,[15–18] and biomedical procedures such as endoscopy or colonoscopy.[19–21] However, mimicking the precise and fast motility of soft-bodied invertebrates using peristaltic locomotion, e.g., slugs, larvae, and earthworms, remains challenging, due to slip as a result of poor segment coordination,[9,22] lack of segmental control precision as a result of segment variations,[23] and the fact that the stiffness of materials and/or structures exploited in artificial worms is much higher than in living species.[24] Indeed, earthworm-like robots have so far rarely taken advantage of inherently soft stimuli-responsive materials for actuation, but instead largely relied on traditional actuation strategies, such as pneumatic actuators,[19] shape-memory alloy (SMA) springs,[25,26] and servomotor-driven tendon systems,[23,27] which all offer precise actuation control and large actuation force. Wormlike robots based on such semirigid designs exhibit some flexibility but they contain stiff parts.[28–30] Such robots contributed to a better understanding of peristalsis and led to advanced models of worm locomotion.[11,23,31] However, the rigid parts (e.g., compressors, SMA springs, or servomotors) used to assemble such systems limit their mechanical compliance. While alternative actuation strategies based on different stimuli-responsive soft materials, such as liquid metals,[32] magnetic fluids,[33] hydrogels,[34] or dielectric elastomers,[35–37] have been explored for peristaltic locomotion, they typically offer little functionality beyond basic locomotion in predefined environments (e.g., tubes) and lack the actuation precision, scalability, and resilience to achieve effective motility observed in wormlike organisms. Thus, worm robots appear to be either functional or soft; a tendency that is also shared by recently reported bending actuators.[24] For instance, multilayered bending actuators based on SMA wires embedded in an elastic matrix have limited mechanical compliance due to the comparatively thick SMA wire.[38] Ionic polymer–metal composites, as another example,

L. F. Muff, V. Buclin, A. Roulin, C. Weder
Adolphe Merkle Institute
University of Fribourg
Chemin des Verdiers 4, Fribourg CH-1700, Switzerland
E-mail: christoph.weder@unifr.ch
A. S. Mills, S. Riddle, H. J. Chiel, R. D. Quinn, K. A. Daltorio
Case Western Reserve University
Cleveland, OH 44106, USA
E-mail: hjc@case.edu; rdq@case.edu; kam37@case.edu
The ORCID identification number(s) for the author(s) of this article can be found under https://doi.org/10.1002/adma.202210409.

DOI: 10.1002/adma.202210409

have a soft body but often fail to produce the forces necessary to operate robots with dimensions on the cm scale.[39,40] Recent advances in the understanding of the underlying principles of peristaltic locomotion help to rationally design actuation systems based on novel soft materials for earthworm robots that are soft and functional.[11]

Here, we report the first earthworm-like robot that is exclusively composed of soft bilayer actuator segments. These elements offer large bending forces and are assembled in a modular manner. The bilayer bending actuators contain integrated Joule heaters and a newly developed semicrystalline polyurethane with an exceptionally large nonlinear thermal expansion coefficient. This design provides the robot with a soft body. The inherent mechanical compliance of the robot allows itself to squeeze through and adapt to tight spaces that are smaller than its unimpeded minor diameter, which is an important task that many traditionally rigid robots struggle with or are unable to perform entirely. In addition, soft robots have been shown to improve safety in human interactions,[41] exhibit high resistance to being damaged,[42] and recover their original shape after significant external impacts.[43]

2. Results and Discussion

The earthworm-like soft robot reported here consists of electrothermally controlled segments of axially joined bilayer bending actuators. These elements comprise a thermoplastic, polyurethane elastomer (PEG-PU) as high-thermal-expansion material, a low thermal expansion polyimide (PI) layer, and a 1 µm thin, compliant copper layer as an integrated Joule heater between the two polymer layers. The metal electrodes employed are so thin that their use does not change the mechanical properties of the polymer bilayer in a significant manner and the elements produced by such a combination remain soft. The PEG-PU employed in this study was designed based on a recently reported approach to create polymers displaying large coefficients of linear thermal expansion (CLTE) in a narrow temperature range.[44,45] The polyethylene glycol (PEG) blocks form semicrystalline domains, while the hard blocks containing the urethane groups act as physical crosslinks. The polymer softens and a large nonlinear thermal expansion is observed upon heating and melting of the PEG crystals, but the material liquefies only at a much higher temperature, where the urethane hard phase dissociates. Thus, the operating principle of the bilayer actuators relies on electrothermally heating them above the melting temperature (T_m) of the PEG domains and translating the large thermal expansion of the PEG-PU layer into a bending motion. Subsequent cooling below the crystallization temperature (T_c) of the PEG domains reverts the actuation. The specific material utilized here was synthesized according to a recently reported protocol.[45] Based on the reported structure-property relations of PEG-PUs, and with the goal to optimize thermal expansion, the PEG-PU employed here was synthesized by the reaction of hydroxyl-terminated PEG with a number-average molecular weight (M_n) of 10 kg mol^{-1}, 7 wt.% 1,4-butanediol (BDO) as chain extender, and 1,6-hexane diisocyanate. The resulting PEG-PU had an M_n of 41 kg mol^{-1}, as determined by size-exclusion chromatography. Its chemical structure was confirmed by proton nuclear magnetic resonance (^{1}H-NMR) spectroscopy (Figure S1, Supporting Information) and Fourier-transform infrared (FT-IR) spectroscopy (Figure S2, Supporting Information). The melting and crystallization temperatures of the PEG domains are T_m = 55 °C and T_c = 30 °C, respectively (Figure S3a, Supporting Information), the thermal expansion in the temperature interval from 25–65°C is α = 2.1% (Figure S3b, Supporting Information), the storage moduli below and above T_m are E' = 477 MPa (25 °C) and E' = 11 MPa (65 °C), respectively (Figure S3c, Supporting Information), and the Young's modulus at 25 °C is E = 361 MPa (Figure S3d, Supporting Information).

To model the bending behavior of PEG-PU/PI bilayers, a modified Timoshenko equation was used, which uses the temperature-dependent CLTE of the PEG-PU and the elastic moduli of the two materials as inputs (Equation S3, Supporting Information). The model was used to predict the curvature and bending behavior of PEG-PU/PI bilayer actuators as a function of layer thickness. Based on the commercial availability of PI films and considering an adequate stiffness of the elements for the targeted scale of the robot (vide infra), the thickness of the PI layer was fixed at 125 µm. Based on this value, the model predicts that the maximum curvature is attained with a 200–300 µm thick PEG-PU layer (**Figure 1**a).

Individual worm segments can be conjoined axially in a modular manner with other segments (Figure 1b). These segments were dimensioned based on design parameters that include the bilayer radius of curvature (R_0), the bilayer arc measure or design angle (θ), the initial segment length (L_0) during the resting state, the fully actuated segment length (L_f), the connection pad length (L_c), and the bilayer width (w). The connection pad is used to join individual segments and to connect wires to the exposed electrode pads of the Joule heater and it remains flat during actuation (**Figure 2**a). To select the optimal design parameters, an analysis was performed based on the traveling wave method for heat-actuated worm locomotion, where slip is avoided by equating the total rate of length change of all activating (heating) portions of the worm with the total rate of length change of all relaxing (cooling) portions of the worm.[11] A linearization of this constraint (Equation S7, Supporting Information) was used to predict the velocity (Equation S8, Supporting Information) and the cost of transport (COT, Equation S9, Supporting Information) of the robot. Previous experiments with electrothermally driven bilayer bending actuators have shown that an energy of ≈0.108–0.149 J mm^{-3} is required to fully melt the crystalline PEG-PU domains to achieve full actuation.[45] In addition, it was found that this process becomes more energy efficient at lower heating rates.[45] Using the lower boundary as a requirement for the activation of an individual bilayer, the non-slip constraint, and the curvatures predicted by the modified Timoshenko model, an analysis of a theoretical six-segment worm as a function of θ and PEG-PU layer thickness was performed. The results show that for a given L_o, the velocity and COT (Figure 1c; Figure S4, Supporting Information) can be optimized with a PEG-PU layer thickness that affords the highest curvature or inverse R_o (Figure 1a) and by selecting a θ of 90° (Figure S4, Supporting Information).

Through use of the geometric relations of the worm segment (Figure 1b; Equation S4, Supporting Information), setting the

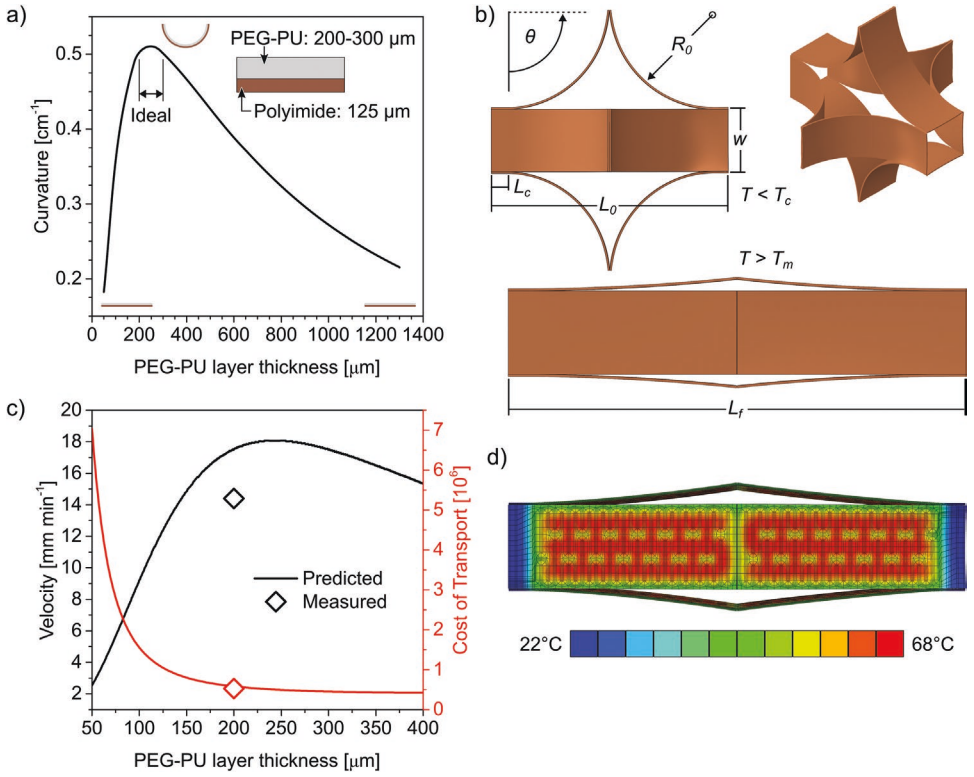

Figure 1. a) Predicted curvature of a PEG-PU/PI bilayer as a function of PEG-PU layer thickness; the thickness of the PI layer was fixed at 125 µm. b) Geometric design parameters of the worm segment. c) Predicted worm velocity (black line) and cost of transport (red line) as a function of PEG-PU thickness; the thickness of the PI layer was fixed at 125 µm and the bilayer section length with connection pads was set to 33 mm. The experimentally determined values for PEG-PU/PI bilayers (layer thickness of PEG-PU = 200 µm and PI = 125 µm) are shown as diamonds. d) FEA nodal temperatures (given as °C) for the selected worm segment design under gravitational field during heating. Encastre boundary conditions were applied to all the connection pad external faces on the left side of the worm segment.

PEG-PU layer thickness to 200 µm, which is at the lower end of the optimal curvature range, along with using a θ of 90°, results in a 29.5 mm bilayer arc length (S), which using a L_c of 3.5 mm, results in a L_0 of 66 mm. These segment dimensions along with a w of 12 mm were used for the fabrication of a worm robot (vide infra) and further finite element analysis (FEA) modeling. The FEA model simulated the transient thermomechanical bilayer response and incorporated gravitational sagging effects as well as the Joule heater circuitry geometry. Using this model it was possible to verify that the proposed bilayer segment does not excessively sag under its own weight (Figure 1d) and to predict the actuation performance of the worm segments (**Figure 3**a,d). Further details of the FEA and material data used can be found in the supporting information (Tables S1–S4 and Figure S5, Supporting Information).

Worm segments based on the above-described design were assembled by joining two elements that each contain four connected bilayer actuation sections (Figure 2a-c). Each segment was produced as follows (for details, see Experimental Section). First, a thin (≈1 µm) copper layer was deposited via physical

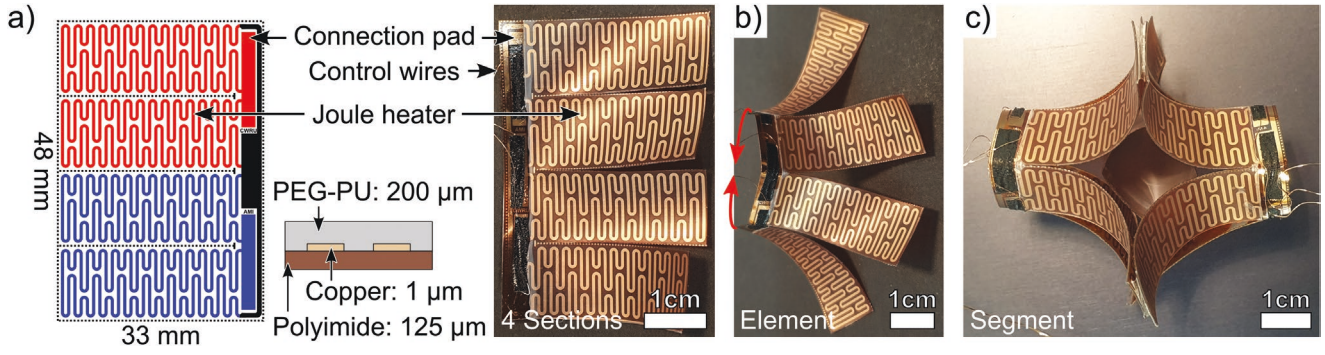

Figure 2. a) Schematic and picture of an element of the worm segments reported. The element features four connected Joule heating electrodes that define four actuation sections. The circuitry is parallel for two section pairs and allows activating these pairs (red and blue) separately by applying a current between pads red and black, or blue and black. b) The elements are folded and fixed (b, red arrows). c) Two elements are joined to form a segment.

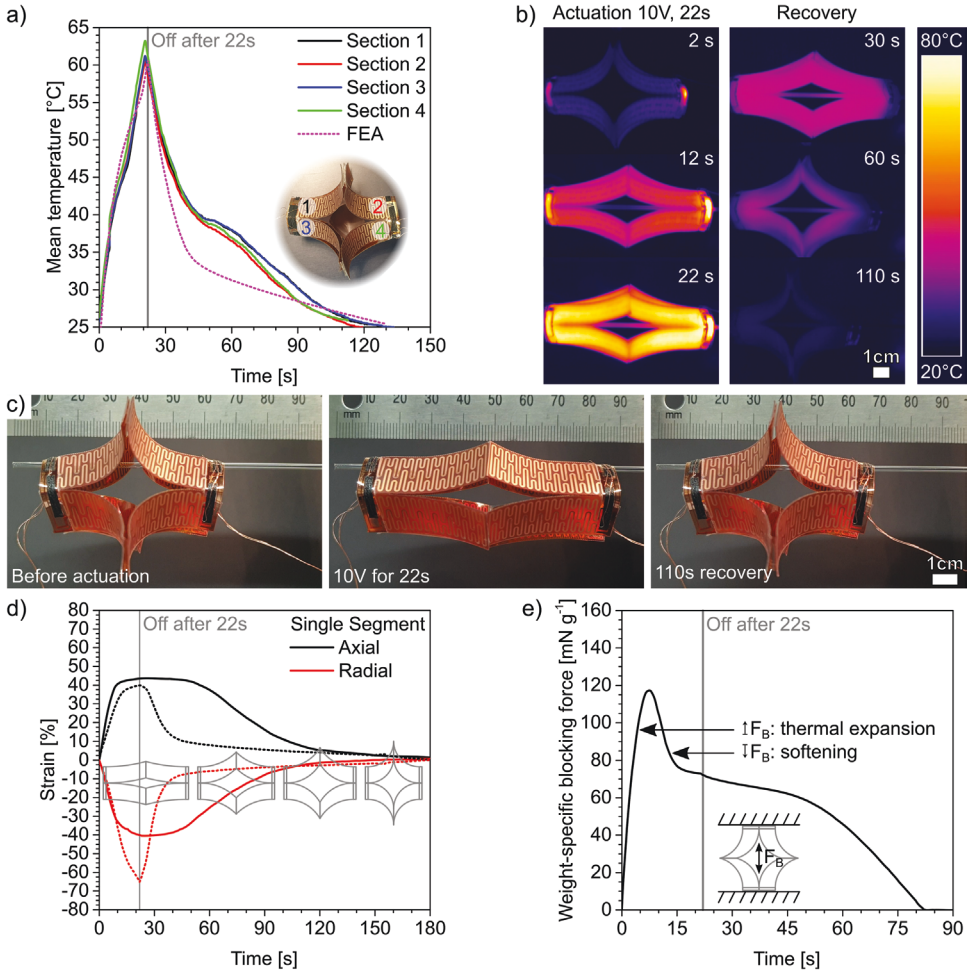

Figure 3. a) Plot of the mean temperature and b) thermal images of four visible actuation sections of one worm segment during actuation and subsequent recovery; in (a) the trace predicted by FEA is also shown. c) Pictures of a single worm segment before actuation (left), in the fully activated state (middle), and the fully recovered state (right) from. d,e) Plots showing the measured (full line) and predicted by FEA (dotted line) axial (black) and radial (red) strains (d) and the weight-specific blocking force against time (e). Experimental data were acquired during actuation with a voltage of 10 V over the course of 22 s and subsequent recovery.

vapor deposition onto a PI film and the Joule heater electrode pattern (≈30 Ω for each actuation section) was etched into the deposited copper layer using a photolithographic process. The Joule heater design (Figure 2a) features three connection pads for thin copper wires (⌀ = 0.5 mm), which allow one to control two pairs of actuation sections that are connected in parallel (red and blue). A 217 ± 26 µm thick PEG-PU film was then compression-molded at 140°C for 1 min with a load of 4000 kg onto the PI film (PI thickness: 125 µm), covering the Joule heater and leaving the connection pads exposed to connect the control wires. To control the bilayer thickness, a 400 µm metal insert was used during compression molding (for details, see Experimental Section). The bilayers were left to cool for 30 min before further processing, to ensure complete crystallization of the PEG. As a result of this process, the bilayers curved upon cooling. Cuts were applied between the four actuation sections in each element (Figure 2a, photograph), and the elements were folded into a circular manner (Figure 2b) and fixed with adhesive tape. Finally, two of these elements were joined to form a full segment (Figure 2c). This was accomplished with four strips of adhesive tape, which serve as hinges between the actuator sections.

The optimal driving voltage to actuate the segments, which in turn governs the heating rate and actuation time, was determined with a six-segment robot in mind (vide infra) and based on the premise that only one of the segments would be activated at any time to allow sufficient cooling time prior to re-actuation. Proper adjustment of the voltage is important to rapidly melt the PEG domains and to avoid significant overshooting of the temperature above T_m, which would lead to an increased recovery time. Furthermore, it is critical to achieve homogeneous heating and to avoid temperature gradients, in order to synchronize the flattening or bending of axially connected sections and to prevent the buildup of internal stresses. The Joule heating electrode was designed for operation with commercially available electronics and microcontrollers that commonly operate in a range of 5–12 V and allow a direct current of up to 2 A. Based on exploratory experiments, copper electrodes with copper lead length of 309 mm, a width of 0.5 mm, and a thickness of 1 µm were used, and a driving voltage of

10 V was chosen. We note that the electrode dimensions can be adjusted to tune its resistance for operation at higher or lower voltages.[46] When operated at a voltage of 10 V, an activated segment (with all eight actuator sections switched on) draws a current of ≈1.2 A, which corresponds to a power of 12 W. Figure 3a and Movie S1 (Supporting Information) show that full actuation (T_m = 55 °C) of a segment can be achieved under these conditions in ≈17 s, whereas a cooling time of ≈110 s is required to return to ambient temperature (Figure 3a,b). To reach this time and ensure full actuation, each activated segment was powered slightly longer than necessary (22 s), and this brought the temperature of its actuating sections to 60 ± 1 °C (Figure 3b,c). These operating conditions translate into an activation energy of 265 J per segment and thermal images show that large temperature gradients can be avoided (Figure 3b). After cutting the power, the temperature instantaneously drops and reaches T_c of the PEG-PU (30°C) after ≈65 s (Figure 3a,b).

The FEA results match the measured temperature until the crystallization of the PEG domains sets in, but the release of the heat of fusion, which was not considered in the FEA, slows down the cooling process beyond this point. The time, until the segment has returned to ambient temperature, is ≈110 s (Figure 3b,c). Note that cooling to ambient temperature (≈110 s, T = 25 °C) is significantly slower than heating to full actuation (≈17 s, T_m = 55 °C). Thus, the actuation speed is limited by the cooling step, which in turn depends on the actuator's geometry. It was found that thinner bilayer bending actuators cool 1.2 and 3.5 times faster for bilayer thicknesses of 225 and 75 µm in comparison to the bilayers (thickness = 350 µm) used in this work (Figure S6, Movie S2, Supporting Information). Plots of the radial and axial strains (Figure 3d) and the weight-specific blocking force (Figure 3e) against time show that the axial and radial motions reach a plateau after 7 s of actuation. The weight-specific blocking force also peaks after 7 s at ≈115 mN g^{-1}, before it drops to 75 mN g^{-1}, due to the reduction of the modulus of the PEG-PU layer caused by the melting of the PEG domains (Figure S3c, Supporting Information). The durability of individual PEG-PU/PI bilayer bending actuators has previously been investigated with no significant loss in blocking force over 250 actuation cycles.[45] Furthermore, SEM micrographs of the bilayer cross-section show no indication of delamination or microcrack formation after 250 cycles (Figure S7, Supporting Information). The full recovery of the axial and radial strains required a bit more time (≈150 s recovery time, Figure 3d) than cooling to ambient temperature (Figure 3a,b), suggesting that the final stage of the recovery process depends on the crystallization and not cooling rate. Interestingly, the FEA results (Figure 3d) show an overestimation of the radial strain and a slight underestimation of axial strain, possibly due to unintended stresses and misalignments that are caused by the manufacturing process which produce somewhat imperfect bilayers with varying radii of curvature.

Six individual worm segments with a maximum weight-specific blocking force of 94 ± 27 mN g^{-1} (Figure S8, Supporting Information), all prepared as reported above, were assembled into a six-segment robot. Because of its waveform, i.e., all segments being in motion at all times (five contracting and one expanding), the robot requires anisotropic friction to achieve directional locomotion.[11] Mimicking the strategy used by earthworms (*Lumbricus terrestris*) to prevent backward sliding, we, therefore, equipped the worm with twelve setae (two for each segment, attached with adhesive tape) that were manufactured from PI and applied between two actuation sections (**Figure 4**a inset). Based on the data shown in Figure 3, the robot was operated by continuous peristaltic actuation; the segments were sequentially activated by applying 10 V for 22 s, which allowed a recovery period of 110 s before the next activation (Figure 4a). To operate the robot, a custom control circuit was assembled, which allowed timed feedforward-type operation using a programmable microcontroller (Figure S9 and Code S1, Supporting Information). In anticipation of future feedback-type operations, we integrated the capability to measure the resistance of the Joule heaters, which changes slightly during actuation (see Experimental Section for further details). Figure 4b and Movie S3 (Supporting Information) demonstrate that the worm equipped with setae is capable of directional locomotion with a speed of up to 13 mm min^{-1}, whereas locomotion of the same robot without setae was ineffective (Figure 4b; Movie S4, Supporting Information). Owing to its compliant structure, the worm-like robot can navigate terrains with diverse surface properties and textures. To demonstrate this intriguing capability, its locomotive performance was investigated on different surfaces, including a paper sheet, nubby and flat rubbery mats made from poly (ethylene-*co*-vinyl acetate) (PEVA), a low-friction Teflon film, and a polyurethane foam (Figure 4c; Movies S5–S8, Supporting Information). The fastest motion was observed on paper (13 mm min^{-1}), followed by the nubby PEVA surface (10 mm min^{-1}). The performance on smooth, sticky PEVA or extremely slippery Teflon was similar, with a velocity of 6 mm min^{-1}. The slowest motion (4 mm min^{-1}) was observed on a porous polyurethane foam block, in which case the pointy setae penetrate the foam structure and get jammed. We anticipate that better multi-substrate performance can be attained by improved setae design.[47,48]

The ability to turn a robot and steer it in a specific direction is vital for terrestrial navigation. For earthworm-like robots, turning and steering require nonperiodic waveforms that allow the machines to orient themselves.[49] The elements in the current robot are designed so that the Joule heaters (or the sections) in the segments can be controlled in pairs (Figure 2a), and this allows one to activate the two sides of each segment (left or right in axial direction) independently. Thus, the worm robot curves at a given segment in response to actuation of a specific side (**Figure 5**a; Movie S9, Supporting Information). Turning on the spot can be achieved by using the front segment as an anchor, which is first lifted (i.e., radially contracted by actuation) and subsequently moved to the side by the simultaneous onesided actuation of the second and third segments. The back half of the robot is oriented by sequential actuation of the 4th, 5th, and then 6th segments, while the front segment acts as an anchor to minimize sideways slip (Figure 5b; Movie S10, Supporting Information). Steering (i.e., turning during forward locomotion) can be achieved with an 11 s (i.e., half of the actuation time) actuation offset between the two sides, i.e., one side is actuated earlier than the other (Figure 5c; Movie S11, Supporting Information). With both strategies, a directional change of ≈3° for each completed nonperiodic wave can be achieved (Figure 5b,c).

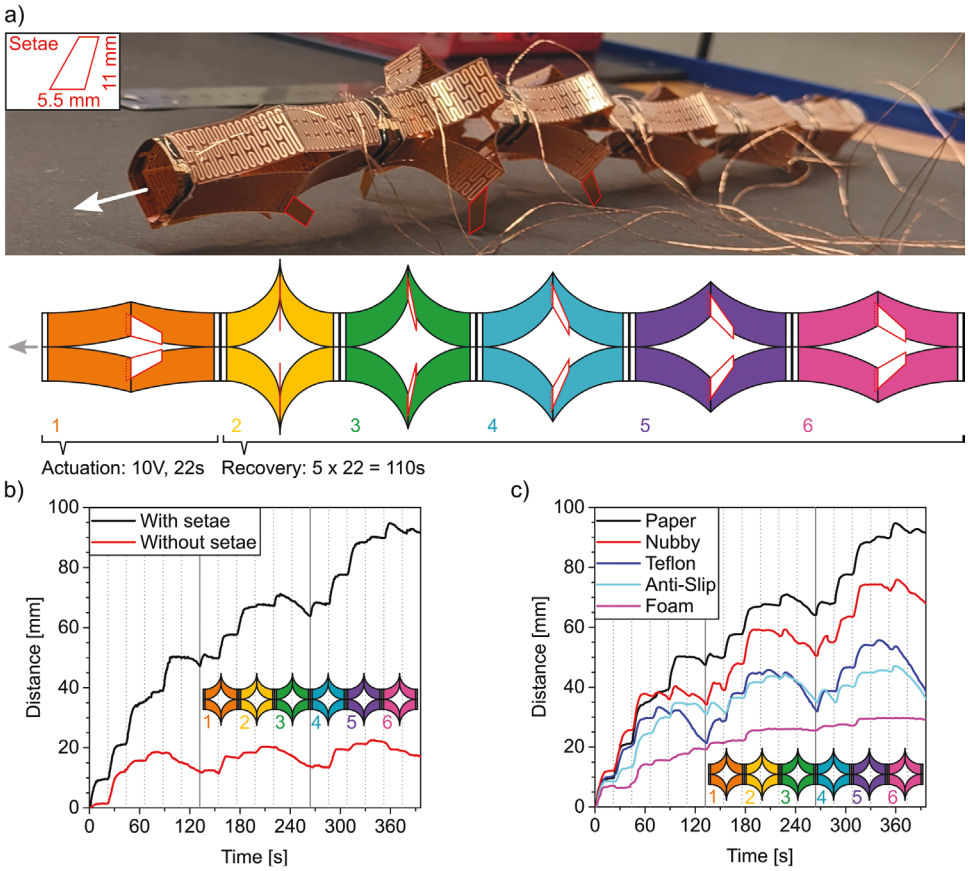

Figure 4. a) Photograph and schematic representation of the soft worm-like robot with PI setae (inset and parts framed in red). The first segment is activated and suspended in air. The schematic shows the timed actuation periods of the various segments (10 V for 22 s). The actuation sequence is numbered and color-coded. b) Plot of the distance covered by worm robots with (black, Movie S3, Supporting Information) and without (red, Movie S4, Supporting Information) setae on paper as a function of time. c) Plot of the distance covered by a worm robot with setae on selected surfaces (see text, Movies S5–S8, Supporting Information).

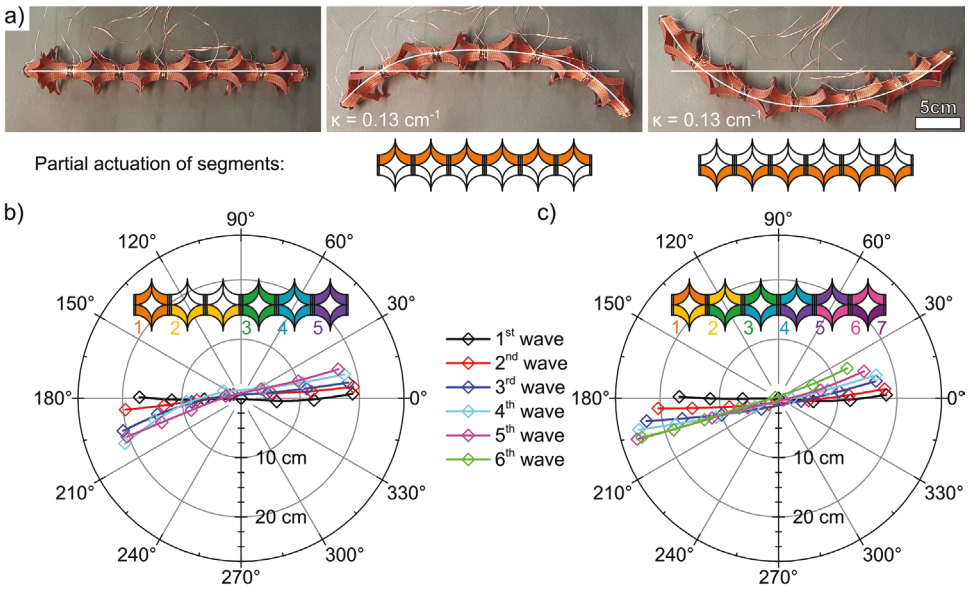

Figure 5. a) Pictures showing the worm-like robot in straight and curved configurations. The latter is attained by actuation of either all right or left sides of all segments. b,c) Polar plots showing the positions of the segments of the robot upon turning on the spot (b) (Movie S10, Supporting Information) and a left-steered forward motion (c) (Movie S11, Supporting Information) by nonperiodic waveforms as indicated by numbers and colors.

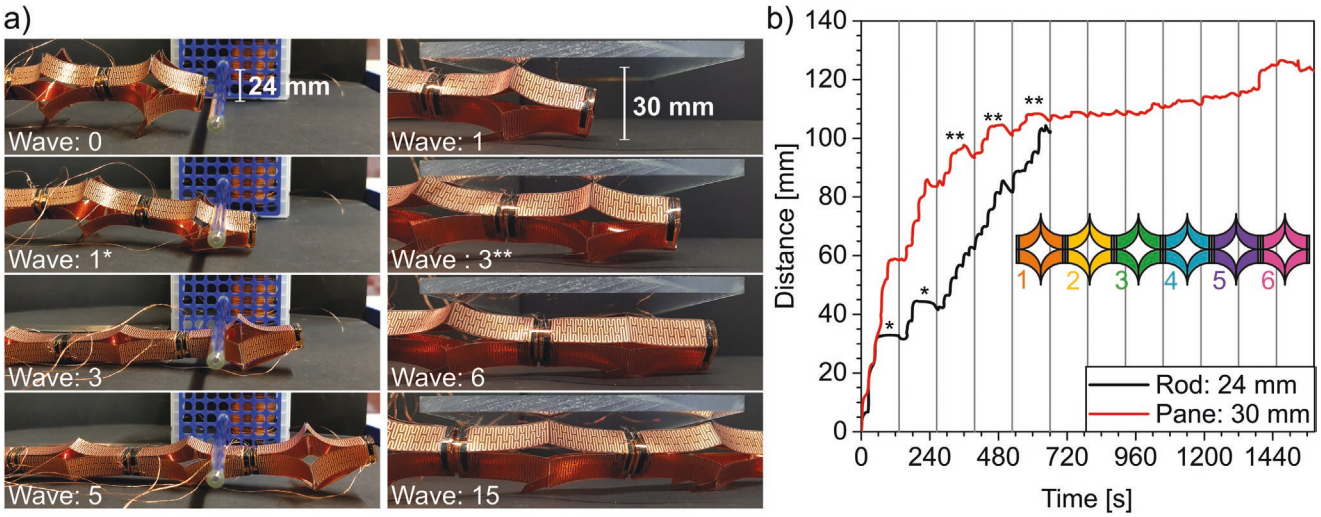

Figure 6. a) Pictures showing the worm-like robot squeezing itself through a spatially constricted space smaller than its resting height (≈44 mm), i.e., underneath a glass rod (left) or an acrylic glass pane (right). b) Plot of the distance covered by the worm underneath the rod (black) or the pane (red) as a function of time. Situations, where forward locomotion is blocked by an obstacle, are indicated by * (rod) and ** (pane).

Because the worm-like robot is mainly composed of soft materials (PEG-PU and PI), it can adapt to and overcome obstacles in unknown terrain. Most remarkably, the robot can squeeze through narrow spaces that are much tighter than its resting height (≈44 mm). It can also advance over long distances (>10 cm) under vertical restrictions without modification of the simple periodic waveform used for unidirectional locomotion (**Figure 6**a; Movies S12 and S13, Supporting Information). When the path of the soft bilayer worm is blocked, it continues to push against the obstacle until it can conform around or squeeze underneath it. Under spatial restriction (i.e., a glass rod or an acrylic glass pane, Figure 6a,b) the speed of the peristaltic locomotion is reduced (i.e., 9 and 3 mm min^{-1} for the rod and pane, respectively) and thus the actuation efficiency is lower until the obstacle is overcome (Figure 6b).

In the context of potential applications in search and rescue operations, robots may encounter situations in which they are suspended vertically. In such scenarios upward or downward movements are essential, for example, to allow the worm to explore its environment with auxiliary sensors or to deliver or pick up cargo with auxiliary grippers. We demonstrate that the robot reported here can tilt its head up to an angle of 45° (**Figure 7**a; Movie S14, Supporting Information) and can extend by up to 20% to close gaps or approach its target (Figure 7b; Movie S15, Supporting Information).

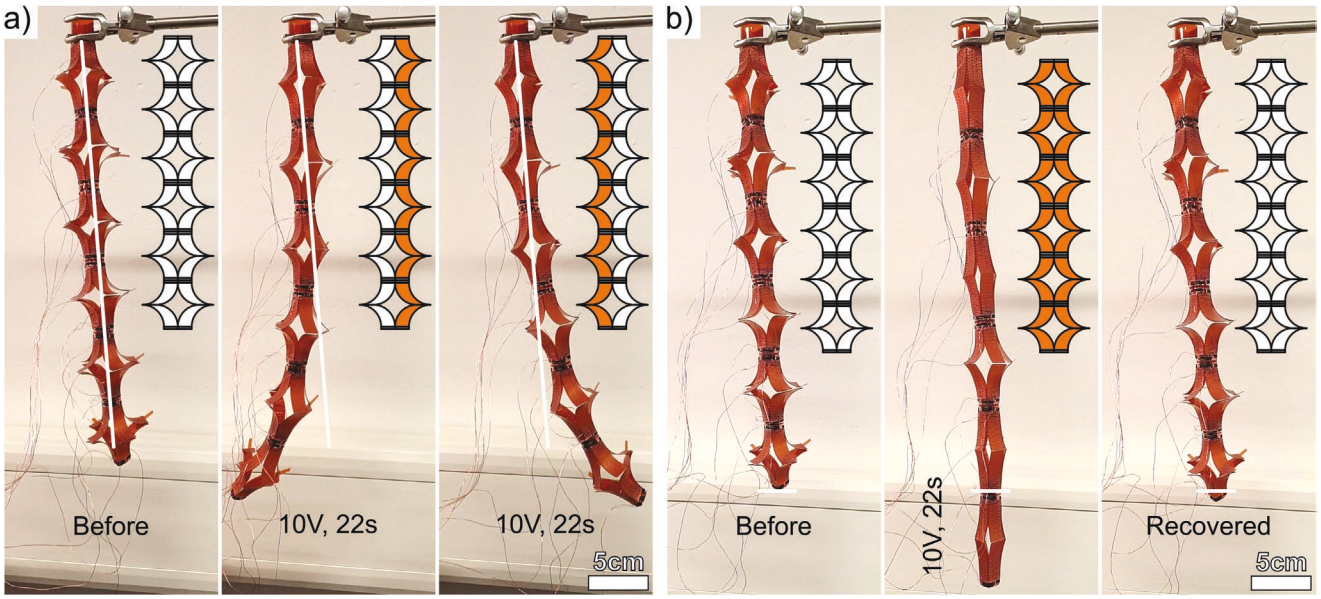

Figure 7. Picture series of vertically suspended worm robot demonstrating sideways head tilting (a) and vertical extension (b). Cartoons show which bilayer elements are powered (orange; 10 V, 22 s) and off (white).

3. Conclusion

We used PEG-PU as high-thermal-expansion material to fabricate bilayer actuator elements with integrated Joule heaters, which in turn were assembled into segments that were used to construct a fully modular and soft earthworm-like robot. Both the segment and the worm designs were augmented by computer simulations and FEA to optimize the actuation properties taking into consideration locomotion velocity and cost of transport. Equipped with artificial setae, directional locomotion on different surfaces was achieved. While directional locomotion is generated with a simple periodic waveform, it is also possible to selectively activate the left or right side of each segment, and this allows one to steer the robot in the desired direction and control various other motions. We demonstrated that the worm robot presented here can overcome constrictions smaller than its unimpeded minor diameter and squeeze itself through a long narrow passage.

Furthermore, our bilayer worm segments generate a maximum weight-specific blocking force of 115 mN g^{-1} (Figure 3e) that outperforms recently reported multilayer bending actuators based on shape memory alloy (54 mN g^{-1}),[38] or on ionic polymer-metal composite (30 mN g^{-1}).[50,51] In addition, it is notable that a lower relative metal thickness for Joule heating is used in the PEG-PU/PI bilayer elements (0.3%, Figure S10a, Supporting Information) than in the aforementioned bending actuators based on shape memory alloy (15%, Figure S10b, Supporting Information),[38] and ionic polymer-metal composite (1%, Figure S10c, Supporting Information).[50,51] Although this comparison is focused on the actuator cross-section and does not take into account the geometry of the Joule heater, it allows for a rough estimation of the metal content in bending actuators. The incorporation of metal in soft robotic systems is often unavoidable for the execution of intended tasks but undesired due to the metal's comparably high rigidity. Thus, we argue that a very thin metal layer (0.3% of the bilayer thickness) did not overly stiffen the worm robot, which allowed it to squeeze through confined spaces.

We recognize that the first embodiment of the worm design is characterized by limited speed (currently <0.1 body lengths per min on all terrains) and a high COT. However, these parameters are largely driven by the electrothermal activation mechanism that we exploited. Moreover, the limited speed and high operating voltage are directly related to the dimensions of the actuating elements. Consequently, we expect that the performance can be greatly improved – without changing the overall design – by utilizing faster and more energy-efficient bending actuators, either based on further improved high-thermal-expansion materials, re-dimensioning of the actuating elements, or alternative energy conversion principles, such as, for example, bending actuators based on dielectric elastomers.[52–55]

In the last few years, a variety of new approaches have been developed for generating oscillatory behavior for novel soft robots, using a wide variety of novel materials,[56–58] some of which are actuated using an external light source or magnetic field.[59,60] Arranging such inputs in a search and rescue or exploratory context may be challenging. In the current robot, autonomy may be achieved by the incorporation of (soft) batteries, which would be lighter and less bulky than a pneumatic source. In conjunction with the addition of soft control systems, these changes would eliminate the need for tethers entirely.

The modular design approach presented here allows one to readily change the structure of the robot. For example, it is readily feasible to increase the number of segments to investigate and optimize alternative wave patterns to decrease the COT and increase the velocity, which in worm robots generally scales with length.[11] The modular design is also expected to facilitate the implementation of auxiliary features, such as sensors, grippers, and other active elements. For instance, the copper Joule heating electrode could double as a temperature sensor by measuring the temperature-dependent resistivity change during actuation, which would allow closed-loop control to optimize heating and cooling time. Finally, the bilayer worm also sets itself apart from other earthworm-like robots in that it features a completely hollow body design, which might be suitable for bidirectional cargo transportation within the worm robot's body.

4. Experimental Section

PEG-PU Synthesis: The PEG-PU was prepared from PEG (10kPEG: 8.21881 from Sigma Aldrich with an M_n of 10.5 kg mol^{-1}) 1,4-butanediol (7 wt.%), and 1,6-hexane diisocyanate as reported elsewhere.[45] The M_n of 41 kg mol^{-1} was lower than that of the corresponding material that was previously reported and therefore the properties of the materials were slightly different.

Joule Heater Patterning: A PI film (thickness: 125 µm from Goodfellow) was coated with a thin (≈1 µm) copper film using a physical vapor deposition system from Inficon with an SQC 310 deposition controller, using Cu pellets with 99.99% purity (Kurt J. Lesker Company). The copper layer was coated with AZ ECI 3007 positive photoresist from Microchemicals on an SM 150 spin coater from Sawatec at 2000 rpm and subsequently soft-baked for 1 min at 90 °C on a Sawatec HP 150 heating plate. The photoresist was selectively irradiated in a UV chamber (365 nm) from Hönle AG using a custom-made photomask from SELBA S.A. for 14 s at a power of 10 mW cm^{-2} (140 mJ cm^{-2}). After exposure, the PI film was developed in a solution of 1:1 H2O:AZ Developer from Microchemicals for 2 min and finally etched in 0.1 M ammonium persulfate for ≈2 min. The copper-patterned PI film was rinsed with deionized water after each step and the photoresist was removed with acetone to expose the copper Joule heating electrode, which was connected to an enameled copper wire (⌀ = 0.5 mm) with conductive copper or carbon tape.

Film and Bilayer Preparation: A benchtop manual press with electrically heated plates (Model 4386) from Carver Inc. was used to prepare PEG-PU films and PEG-PU/PI bilayers. The PEG-PU (vacuum dried at 70 °C, overnight) was compression-molded between two Teflon sheets (thickness: 0.15 mm from Goodfellow) for 1 min under a load of 4000 kg at 140 °C. Stainless steel inserts were used to produce films for thermomechanical testing (insert thickness: 0.25 mm) as well as bilayers (insert thickness: 0.4 mm). To produce bilayers, the PEG-PU was compression-molded onto a PI film (bilayer thickness: 342 ± 26 µm, PEG-PU thickness: 217 ± 26 µm, and PI thickness: 125 µm from Goodfellow). The hot films and bilayers were removed from the press with and between the Teflon sheets and allowed to cool at ambient temperature (25 °C). Bilayers were stored at 20 °C and 40% relative humidity.

Worm Segment Fabrication: The compression-molded bilayer elements were cut with scissors (along the dotted lines, Figure 2a) to obtain four connected bilayer actuation sections. Thin enameled copper wires (⌀ = 0.5 mm) with exposed ends (enamel burnt off with solder)

were connected to the electrode pads with conductive carbon tape from Micro to Nano. Two such elements were joined together with adhesive tape (thickness: 60 µm, Scotch Transparent from 3M) applied to the PI side of all four actuation sections and subsequently folded along the cut lines of each section. The fold was secured with adhesive tape (thickness: 60 µm, Scotch Transparent from 3M) to form a worm segment (Figure 2c). All segments were stored and actuated at 20 °C and 40% relative humidity.

Segmented Worm Assembly: The worm segments were joined with a rectangular piece of PI (thickness: 125 µm) folded into a square-shaped tube (length: 15 mm) that acted as a connection piece with slightly smaller dimensions than the actuation section width (12 mm). For additional stability, double-sided adhesive tape (Thickness: 60 µm, Scotch Transparent from 3M) was added to the connection piece before it was plugged into the opening of a segment.

Electrothermal Actuator Operation: A Model 2400 Series source meter from Keithley was used to measure the electronic resistance of the individual actuation sections (≈30 Ω). Individual segments or the six-segmented worm robot were either powered directly or via a control circuit (Figure S9, Supporting Information) with a PPS1600S laboratory power supply from Voltcraft. Individual segments and the assembled worm were stored and actuated under controlled conditions at 20 °C and 40% relative humidity.

Control Circuit Design: The robot was controlled using a circuit built around an Arduino Mega 2560 Rev3 microcontroller. An N-Channel MOSFET (IRLZ34NPBF, Infineon Technologies) was used as a gate to control the power applied to each half of a worm segment, for a total of 12 MOSFETs. Each MOSFET was controlled using a 5 V digital pin on the microcontroller. Following the bilayers, a series of voltage dividers followed by operational amplifiers (LM324N, ON Semiconductor) was used to measure the voltage via the analog pins of the microcontroller. This voltage was used to calculate the current going through the bilayers and their resistance upon being heated. This data was not utilized in the present study, but the capability would be exploited in future studies for control purposes. Further details of the circuit and the code used on the microcontroller can be found in the supplementary information (Figure S9 and Code S1, Supporting Information).

Thermal Imaging: Thermal images were recorded with a PI 160 IR camera from Optris GmbH. The data were evaluated in the Optris PI connect software and visualized with the Origin 2016 software from the OriginLab Corporation.

Motion Analysis: Segment actuation or worm locomotion/maneuvers were captured with a Samsung and/or Google mobile phone camera and converted into .avi file format with a frame rate of 2 fps. These files were then loaded in Tracker version 6.0.10 from D. Brown et al. for automated pixel tracking. A ruler in the background and/or visible features of the electrode pattern were used as calibration points.

Blocking Force: The blocking force of each worm segment was measured with an MS Semi-Micro NewClassic benchtop balance from Mettler-Toledo AG. The segments were positioned on the balance under a fixed surface such that they would press onto the force transducer of the balance during electrothermal actuation. The blocking force was continuously recorded through a serial interface.

Thermal Expansion Measurements: The thermal expansion of compression-molded PEG-PU strips (≈25 × 5.5 × 0.20 mm) was measured on a dynamic mechanical analyzer Q800 from TA Instruments. The strain of the sample was recorded over two melting and crystallization cycles (isothermal at 65 °C and 25 °C for 15 min or with a heating rate of 0.5 °C min^{-1} from 10 to 65 °C) under a constant force of 1 mN. The measurements were conducted in agreement with ASTM E831-06 and the thermal expansion was determined as the difference in strain at 25 and 65 °C.

Differential Scanning Calorimetry: DSC traces of the compression-molded PEG-PU (≈7 mg) were measured from −50 to 130 °C with heating and cooling rates of 10 °C min^{-1} over two cycles, to erase the thermal history, using a STAR system from Mettler Toledo under nitrogen atmosphere. The measured heat flow was divided by the sample weight and the melting (T_m) and crystallization temperature (T_c) were determined by taking the maxima of the melting endotherm and crystallization exotherm.

Dynamic Mechanical Analysis: The dynamic modulus of compression molded PEG-PU strips (≈25 × 5.5 × 0.20 mm) was measured on a dynamic mechanical analyzer Q800 from TA Instruments at 1 Hz with an amplitude of 15 µm from 0 °C with a heating rate of 3 °C min^{-1} until the sample yielded.

Tensile Testing: Tensile measurements were performed on PEG-PU strips (≈25 × 5.5 × 0.20 mm) according to ASTM D1708, at 25 °C, with a static material testing machine from Zwick/Roell equipped with a 200 N Xforce HP load cell. The strain rate was adjusted to 200 mm min^{-1} so that the sample failed after ≈1 min.

Nuclear Magnetic Resonance Spectroscopy: NMR spectroscopy was carried out at a temperature of 24.05 °C in dimethyl sulfoxide-d_6 (DMSO-d_6) on a Bruker Avance DPX 400 spectrometer using a frequency of 400.19 MHz. Spectra were calibrated to the residual solvent peak. Data were evaluated with the MestReNova software suite (version 11.0.1). The molar ratio and weight fraction of BDO and PEG (M_n = 10 kg mol^{-1}) were calculated as the integrals of the peaks at chemical shifts of 3.52 and 1.37 ppm, corresponding to methylene groups of the BDO and PEG residues, respectively.

Fourier-Transform Infrared Spectroscopy: PEG-PU, PEG, and BDO were dried at 70 °C under vacuum for 48 h and HDI was measured as received. Spectra were recorded using a PerkinElmer Spectrum 65 spectrometer with a resolution of 4 cm^{-1} and 4 scans per sample between 4000 and 700 cm^{-1}.

Scanning electron microscopy (SEM): Bilayer bending actuator elements were cut using a razor blade and mounted perpendicular to the SEM sample holder with conductive copper tape. The samples were sputter-coated with a 2 nm thick layer of gold using a Cressington 208HR High-Resolution sputter coater. The secondary electron mode was used to capture the micrographs of the bilayer cross section at 7 kV using a Tescan Mira3 LM FE scanning electron microscope.

Statistical Analysis: Data presented as mean ± standard deviation were calculated using the average and *n*-method of the entire population. Statistical analysis was carried out using Excel and OriginPro Software.

Supporting Information

Supporting Information is available from the Wiley Online Library or from the author.

Acknowledgements

L.F.M and A.S.M. contributed equally to this work. The authors gratefully acknowledge financial support from the Partnerships for International Research and Education (PIRE) program under grant numbers IZPIP0_177995 by the Swiss National Science Foundation (SNSF) and OISE 1844463 by the National Science Foundation (NSF) and the Adolphe Merkle Foundation. The authors also expressed their gratitude to Franziska Marx for her help with the H^1-NMR and FTIR measurements.

Open access funding provided by Universite de Fribourg.

Conflict of Interest

The authors declare no conflict of interest.

Data Availability Statement

The data that support the findings of this study are available from the corresponding author upon reasonable request.

Keywords

bilayer bending actuators, earthworms, earthworm-like robots, phase transitions, phase-changing materials, soft robotics, thermal expansion coefficients

Received: November 9, 2022
Revised: January 25, 2023
Published online: March 22, 2023

[1] B. Chan, S. Ji, C. Koveal, A. E. Hosoi, *J. Intell. Mater. Syst. Struct.* **2007**, *18*, 111.
[2] Z. Ren, W. Hu, X. Dong, M. Sitti, *Nat. Commun.* **2019**, *10*, 2703.
[3] C. Xu, Z. Yang, G. Z. Lum, *Adv. Mater.* **2021**, *33*, 2100170.
[4] C. Laschi, M. Cianchetti, B. Mazzolai, L. Margheri, M. Follador, P. Dario, *Adv. Rob.* **2012**, *26*, 709.
[5] Y. Lee, S. Chun, D. Son, X. Hu, M. Schneider, M. Sitti, *Adv. Mater.* **2022**, *34*, 2109325.
[6] T. Umedachi, V. Vikas, B. A. Trimmer, *Bioinspiration Biomimetics* **2016**, *11*, 025001.
[7] X. Lu, H. Zhang, G. Fei, B. Yu, X. Tong, H. Xia, Y. Zhao, *Adv. Mater.* **2018**, *30*, 1706597.
[8] N. Xia, B. Jin, D. Jin, Z. Yang, C. Pan, Q. Wang, F. Ji, V. Iacovacci, C. Majidi, Y. Ding, L. Zhang, *Adv. Mater.* **2022**, *34*, 2109126.
[9] K. A. Daltorio, A. S. Boxerbaum, A. D. Horchler, K. M. Shaw, H. J. Chiel, R. D. Quinn, *Bioinspiration Biomimetics* **2013**, *8*, 035003.
[10] L. Hu, L. Wang, Y. Ding, S. Zhan, J. Liu, *Adv. Mater.* **2016**, *28*, 9210.
[11] A. Kandhari, Y. Wang, H. J. Chiel, R. D. Quinn, K. A. Daltorio, *Soft Rob.* **2021**, *8*, 485.
[12] B. A Trimmer, A. E. Takesian, B. M. Sweet, C. B. Rogers, D. C. Hake, D. J. Rogers, in Proc. 7th Int. Symp. on Technology and the Mine Problem, Naval Postgraduate School, Monterey, CA, USA **2006**, B457–B467.
[13] A. M. Bertetto, M. Ruggiu, in *2001 IEEE/ASME Int. Conf. on Advanced Intelligent Mechatronics. Proceedings (Cat. No.01TH8556)*, IEEE, Piscataway, NJ, USA **2001**, pp. 1226–1231.
[14] H. Omori, T. Nakamura, T. Yada, *Ind. Rob.: An Int. J.* **2009**, *36*, 358.
[15] M. Ikeuchi, T. Nakamura, D. Matsubara, in *2012 IEEE/RSJ Int. Conf. on Intelligent Robots and Systems*, IEEE, Piscataway, NJ, USA **2012**, pp. 926–931.
[16] K. Harigaya, K. Adachi, T. Yanagida, M. Yokojima, T. Nakamura, in *2013 IEEE Int. Conf. on Mechatronics (ICM)*, IEEE, Piscataway, NJ, USA **2013**, pp. 267–272.
[17] T. Tanaka, K. Harigaya, T. Nakamura, in *2014 IEEE/ASME Int. Conf. on Advanced Intelligent Mechatronics*, IEEE, Piscataway, NJ, USA **2014**, pp. 1552–1557.
[18] R. Ishikawa, T. Tomita, Y. Yamada, T. Nakamura, in *2016 IEEE Int. Conf. on Advanced Intelligent Mechatronics (AIM)*, IEEE, Piscataway, NJ, USA **2016**, pp. 413–418.
[19] E. V. Mangan, D. A. Kingsley, R. D. Quinn, H. J. Chiel, in *Proc. 2002 IEEE Int. Conf. on Robotics and Automation (Cat. No.02CH37292), vol. 1*, IEEE, Piscataway, NJ, USA **2002**, pp. 347–352.
[20] P. Dario, P. Ciarletta, A. Menciassi, B. Kim, *Int. J. Rob. Res.* **2004**, *23*, 549.
[21] K. Wang, G. Yan, *J. Med. Eng. Technol.* **2007**, *31*, 24.
[22] A. S. Boxerbaum, K. M. Shaw, H. J. Chiel, R. D. Quinn, *Int. J. Rob. Res.* **2012**, *31*, 302.
[23] A. D. Horchler, A. Kandhari, K. A. Daltorio, K. C. Moses, J. C. Ryan, K. A. Stultz, E. N. Kanu, K. B. Andersen, J. A. Kershaw, R. J. Bachmann, H. J. Chiel, R. D. Quinn, *Soft Rob.* **2015**, *2*, 135.
[24] A. Kandhari, Y. Huang, K. A. Daltorio, H. J. Chiel, R. D. Quinn, *Bioinspiration Biomimetics* **2018**, *13*, 026003.
[25] B. Kim, M. G. Lee, Y. P. Lee, Y. Kim, G. Lee, *Sens Actuators A Phys* **2006**, *125*, 429.
[26] K. B. Andersen, A. Kandhari, H. J. Chiel, R. D. Quinn, K. A. Daltorio, in *7th Int. Conf., Living Machines 2018: Biomimetic and Biohybrid Systems*, (Eds.: V. Vouloutsi, J. Halloy, A. Mura, M. Mangan, N. Lepora, T. J. Prescott, P. F. M. J. Verschure), Springer International Publishing, Paris, France, **2018**, pp. 6–10.
[27] B. Winstone, T. Pipe, C. Melhuish, M. Callaway, A. C. Etoundi, S. Dogramadzi, in *2016 6th IEEE Int. Conf. on Biomedical Robotics and Biomechatronics (BioRob)*, IEEE, Piscataway, NJ, USA **2016**, pp. 449–456.
[28] T. P. Chenal, J. C. Case, J. Paik, R. K. Kramer, in *2014 IEEE/RSJ Int. Conf. on Intelligent Robots and Systems*, IEEE, Piscataway, NJ, USA **2014**, pp. 2827–2831.
[29] M. C. Yuen, R. A. Bilodeau, R. K. Kramer, *IEEE Robot Autom Lett* **2016**, *1*, 708.
[30] A. Kandhari, A. Mehringer, H. J. Chiel, R. D. Quinn, K. A. Daltorio, *Biomimetics* **2019**, *4*, 13.
[31] K. J. Quillin, *Shi Yan Sheng Wu Xue Bao* **1999**, *202*, 661.
[32] Y. Yao, J. Liu, *RSC Adv.* **2017**, *7*, 11049.
[33] N. Saga, T. Nakamura, *Smart Mater. Struct.* **2004**, *13*, 566.
[34] Z. Sun, Y. Yamauchi, F. Araoka, Y. S. Kim, J. Bergueiro, Y. Ishida, Y. Ebina, T. Sasaki, T. Hikima, T. Aida, *Angew. Chem., Int. Ed.* **2018**, *57*, 15772.
[35] K. Jung, J. C. Koo, J. Nam, Y. K. Lee, H. R. Choi, *Bioinspir. Biomim.* **2007**, *2*, S42.
[36] J. Zhao, J. Niu, L. Liu, J. Yu, *Angew. Chem., Int. Ed.* **2014**, *9056*, 905608.
[37] S. Pfeil, M. Henke, K. Katzer, M. Zimmermann, G. Gerlach, *Front. Rob. AI* **2020**, *7*, 9.
[38] X. Huang, K. Kumar, M. K. Jawed, A. Mohammadi Nasab, Z. Ye, W. Shan, C. Majidi, *Adv. Mater. Technol.* **2019**, *4*, 1800540.
[39] C. Jo, D. Pugal, I.-K. Oh, K. J. Kim, K. Asaka, *Prog. Polym. Sci.* **2013**, *38*, 1037.
[40] M. Shahinpoor, *Electrochim. Acta* **2003**, *48*, 2343.
[41] D. Rus, M. T. Tolley, *Nature* **2015**, *521*, 467.
[42] M. T. Tolley, R. F. Shepherd, B. Mosadegh, K. C. Galloway, M. Wehner, M. Karpelson, R. J. Wood, G. M. Whitesides, *Soft Rob.* **2014**, *1*, 213.
[43] S. Seok, C. D. Onal, K.-J. Cho, R. J. Wood, D. Rus, S. Kim, *IEEE ASME Trans Mechatron* **2013**, *18*, 1485.
[44] L. F. Muff, C. Weder, *Adv. Intell. Syst.* **2020**, *2*, 2000177.
[45] L. F. Muff, C. Weder, *Adv. Intell. Syst.* **2023**, *5*, 2200265.
[46] H. Lu, M. Lei, C. Zhao, Y. Yao, J. Gou, D. Hui, Y. Q. Fu, *Compos B Eng* **2015**, *80*, 37.
[47] T. Manwell, B. Guo, J. Back, H. Liu, in *2018 IEEE Int. Conf. on Soft Robotics (RoboSoft)*, IEEE, Piscataway, NJ, USA **2018**, 54.
[48] B. Liu, Y. Ozkan-Aydin, D. I. Goldman, F. L. Hammond, in *2019 2nd IEEE Int. Conf. on Soft Robotics (RoboSoft)*, IEEE, Piscataway, NJ, USA **2019**, pp. 828–833.
[49] A. Kandhari, Y. Wang, H. J. Chiel, K. A. Daltorio, *Soft Rob.* **2019**, *6*, 560.
[50] L. Yang, D. Zhang, X. Zhang, A. Tian, X. Wang, *Appl. Phys. A* **2020**, *126*, 365.
[51] Q. He, M. Yu, L. Song, H. Ding, X. Zhang, Z. Dai, *J. Bionic Eng.* **2011**, *8*, 77.
[52] F. Owusu, F. A. Nüesch, D. M. Opris, *Adv. Funct. Mater.* **2022**, *2207083*, 2207083.
[53] D. M. Opris, *Adv. Mater.* **2018**, *30*, 1703678.
[54] Y. S. Ko, F. A. Nüesch, D. Damjanovic, D. M. Opris, *Adv. Mater.* **2017**, *29*, 1603813.
[55] S. J. Dünki, Y. S. Ko, F. A. Nüesch, D. M. Opris, *Adv. Funct. Mater.* **2015**, *25*, 2467.

[56] Y. Wu, J. K. Yim, J. Liang, Z. Shao, M. Qi, J. Zhong, Z. Luo, X. Yan, M. Zhang, X. Wang, R. S. Fearing, R. J. Full, L. Lin, *Sci. Rob.* **2019**, *4*, 31.
[57] H.-W. Huang, F. E. Uslu, P. Katsamba, E. Lauga, M. S. Sakar, B. J. Nelson, *Sci. Adv.* **2019**, *5*.
[58] Z. Li, N. V. Myung, Y. Yin, *Sci. Rob.* **2021**, *6*, 4523.
[59] Y. Yang, Y. Liu, Y. Shen, *Adv. Funct. Mater.* **2020**, *30*, 1910172.
[60] X. Du, H. Cui, T. Xu, C. Huang, Y. Wang, Q. Zhao, Y. Xu, X. Wu, *Adv. Funct. Mater.* **2020**, *30*, 1909202.
[61] H. F. Mark, *Encyclopedia of Polymer Science and Technology*, John Wiley & Sons, Hoboken, NJ, USA **2004**.
[62] S. Timoshenko, *J. Opt. Soc. Am.* **1925**, *11*, 233.